

Recombination defects at the 4H-SiC/SiO₂ interface investigated with electrically detected magnetic resonance and ab initio calculations

J. Cottom, G. Gruber, G. Pobegen, T. Aichinger, and A. L. Shluger

Citation: *Journal of Applied Physics* **124**, 045302 (2018); doi: 10.1063/1.5024608

View online: <https://doi.org/10.1063/1.5024608>

View Table of Contents: <http://aip.scitation.org/toc/jap/124/4>

Published by the [American Institute of Physics](#)

Articles you may be interested in

[Band gap tuning of layered III-Te materials](#)

Journal of Applied Physics **124**, 045104 (2018); 10.1063/1.5021259

[Mechanism for the formation of nitrogen-filled voids after annealing of GaN on a sapphire substrate](#)

Journal of Applied Physics **124**, 045304 (2018); 10.1063/1.5039755

[Linear scanning tunneling spectroscopy over a large energy range in black phosphorus](#)

Journal of Applied Physics **124**, 045301 (2018); 10.1063/1.5029571

[Wavefront manipulation based on mechanically reconfigurable coding metasurface](#)

Journal of Applied Physics **124**, 043101 (2018); 10.1063/1.5039679

[Electrically detected magnetic resonance of carbon dangling bonds at the Si-face 4H-SiC/SiO₂ interface](#)

Journal of Applied Physics **123**, 161514 (2018); 10.1063/1.4985856

[Tutorial: Junction spectroscopy techniques and deep-level defects in semiconductors](#)

Journal of Applied Physics **123**, 161559 (2018); 10.1063/1.5011327

AIP | Journal of Applied Physics SPECIAL TOPICS



Recombination defects at the 4H-SiC/SiO₂ interface investigated with electrically detected magnetic resonance and *ab initio* calculations

J. Cottom,^{1,a)} G. Gruber,² G. Pobegen,³ T. Aichinger,⁴ and A. L. Shluger¹

¹University College London—Department of Physics and Astronomy, Gower Street, London WC1E 6BT, United Kingdom

²Institute of Solid State Physics—Graz University of Technology, Petersgasse 16, 8010 Graz, Austria

³KAI GmbH, Europastraße 8, 9500 Villach, Austria

⁴Infineon Technologies Austria AG, Siemensstraße 2, 9500 Villach, Austria

(Received 2 February 2018; accepted 22 June 2018; published online 23 July 2018)

The selectivity of electrically detected magnetic resonance (EDMR) is utilized to probe the dominant recombination defect at the Si-face 4H-SiC/SiO₂ interface. The nature of this defect has long been debated with the two main candidates being the Si vacancy (V_{Si}) or the C-dangling bond (P_{bC}). Through comparison between experimental EDMR measurements and *ab initio* calculations, an important performance limiting recombination defect observed with EDMR in the current generation of nMOSFETs is reasonably explained as a combination of the P_{bC} and the dual- P_{bC} defects. These defects match the symmetry, hyperfine interaction, and isotopic abundance observed in the experimental EDMR spectrum. *Published by AIP Publishing.* <https://doi.org/10.1063/1.5024608>

I. INTRODUCTION

Although SiC based devices offer great potential for high power applications, before this potential can be fully realized there are a number of challenges that must be overcome. One of the main challenges for SiC based metal oxide field effect transistors (MOSFETs) is the poor channel mobility, which remains significantly below the bulk mobility. In addition, threshold voltage instabilities are ubiquitous in SiC MOSFETs.¹ This situation results from the high density of electron traps at the 4H-SiC/SiO₂ interface.^{2,3} Passivation of these traps can be achieved by nitridation, particularly by post oxidation anneals (POAs) in a nitric oxide (NO) atmosphere. Wang *et al.*⁴ described the influence of various POAs on the passivation effect, observing that H effectively passivates deep states while having little effect on the shallow states, where NO is far more effective. However, there is no clear consensus on what the dominant electrically active defects are. Important interface defects in Si MOSFETs have been identified with electron paramagnetic resonance (EPR) many years ago, but for SiC this is not the case. Numerous studies have aimed at identifying those defects by means of EPR and electrically detected magnetic resonance (EDMR), as summarized by Umeda *et al.*^{5–8}

Three defect models are typically relied upon to explain these interface defects: C-clusters, the silicon vacancy (V_{Si}), and the C-dangling bond (P_{bC}).^{9–16} The C-cluster model has been important in the previous generation of devices,^{17–24} but is far less important for the current state-of-the-art where there appears to be no extensive interlayer. This is confirmed by Raman, TEM, and electron energy loss spectroscopy (EELS) studies, showing no significant C-concentration in the interface and near interface region.^{2,24–32} While these methods cannot completely rule out the presences of a C-excess ($[C] < 1\%$) at the interface, it is clear that recently

characterized devices do not show the same C-rich layer that was present in the earlier devices. In itself this would be insufficient to rule out the presence of C-dimer like defects; fortunately, these defects have been extensively studied both experimentally and theoretically.^{33–35} This leaves the V_{Si} and P_{bC} models for consideration in this paper. The P_{bC} center is described and characterized in a series of EPR studies on oxidized porous SiC.^{12,13,34,36} The angular dependence of the differently oriented dangling bonds at the various interfaces was reported to be $g_{\parallel} \approx 2.0023$ when the magnetic field (B) is applied along the symmetry axis of a dangling bond and $g_{\perp} \approx 2.0032$ in the perpendicular direction. The hyperfine (HF) parameters for the P_{bC} center were $a_{C\parallel} \approx 80$ G, and $a_{C\perp} \approx 40$ G for the central C atom, and $a_{Si} \approx 13$ G for the neighboring Si atoms. The negatively charged V_{Si} defect has been identified by EPR in bulk SiC long ago, revealing an isotropic g -factor of $g \approx 2.0028$. The HF parameters due to the four neighboring C atoms are $a_{C\parallel} \approx 28$ G with B applied along the symmetry direction of the unsaturated C-bond and $a_{C\perp} \approx 10.5$ G in the perpendicular direction, as well as $a_{Si} \approx 3$ G for the twelve next neighbor Si atoms.^{8,16,37,38}

Several EDMR studies performed at interfaces produced by thermal oxidation linked the observed defect to the V_{Si} center, based on the isotropic nature of the g -factor.^{11,39,40} The study of Cochrane *et al.*¹¹ resolved the HF structure of the V_{Si} using the adiabatic fast passage EDMR technique. The fast passage technique for EPR measurements was pioneered by Hyde and Weger in the 1960s and 1970s and relates to a scan rate of sufficient speed that the electron spins are not able to relax between modulation sweep cycles.^{11,41,42} However, while this study identified the V_{Si} as the defect observed by fast passage EDMR, the other referenced studies used a conventional detection scheme (without fast passage) and showed a dramatically different spectrum.^{39,40} This is suggestive of a time component to the measurement resulting in different defects probed as a result of

^{a)}j.cottom.12@ucl.ac.uk

the EDMR approach employed. A recent study attempted to rule out the presence of dangling bond defects at the SiC/SiO₂ interface.⁴⁰ This conclusion is based upon the assumption that the observed defect is the V_{Si} defect and not the dangling bond and neglects contributions from more than one (similar) defect. In addition, there is also the device generation challenge that needs to be explored. In particular, early generations of 4H-SiC MOSFETs had a non-abrupt SiC/SiO₂ interface with the presence of a carbon rich SiO_xC_y interlayer.^{24,28} Extensive theoretical and experimental studies allowed for the assignment of a great many of the interface defects to the presence of this excess interface-C.^{3,9,43-46} By contrast, in state-of-the-art 4H-SiC based MOS devices, the interface is devoid of any C-rich SiO_xC_y interlayer and shows an interface that is abrupt but near-continuously stepped.^{24-27,47} As a result of these dramatically different interface morphologies, the distribution between the plateaux and step sites can reasonably be expected to differ significantly. The older generation oxides have an excess of interface-C and large terraces, whereas in the current devices there is no interlayer and the interface is nearly continuously stepped, with the steps aligned along the $\bar{1}100$ direction.^{24-27,47}

The present study aims to establish a theoretical background to interpret the frequently observed EDMR defect signature in SiC MOSFETs. In particular, the V_{Si} in the bulk and at the interface as well as different types of P_{bc} centers was theoretically modeled. Subsequently, the experimental spectra were compared to the simulations. The observations support the assignment to the P_{bc} center, which has recently been suggested.⁴⁸

II. METHODOLOGY

A. Experimental

Different Si-face 4H-SiC *n*-channel MOSFETs with variations in their oxide processes were studied. One device was a MOSFET from an older generation with a thermally grown oxide and a POA in a N₂O atmosphere. The other devices received a state-of-the-art deposited oxide with POAs in NO, N₂O, and O₂ atmospheres. All measurements were performed using the BAE biasing scheme of EDMR.⁴⁹ The source-to-body diode was forward biased at $V_{sb} = -3.5$ V and the gate voltage (V_g) was adjusted for an optimized signal-to-noise ratio. The measurements were performed at room temperature with a microwave frequency of $\omega_m = 9.4022$ GHz, and a magnetic field modulation of $f_{mod} \approx 900$ Hz with an amplitude of $B_{mod} = 1$ G. The full experimental results are presented in Refs. 27, 48, and 50, and the highlights are presented here to facilitate the comparison with the theoretical results. The intensities of the HF plots have been normalized for clarity and ease of comparison with the theoretical results. In contrast to EPR, the intensity is a measure of recombination efficiency and hence no information on concentration can be obtained.

B. Theoretical

DFT calculations were performed using the CP2K code,⁵¹ and the functionals selected for the calculations were

PBE and HSE06.⁵²⁻⁵⁴ These functionals were utilized with the DZVP-MOLOPT-SR-GTH and the TZVP-MOLOPT-GTH basis sets.^{51,55-57} All parameters were converged to 0.01 meV per formula unit, leading a plane wave cutoff of 650 Ry. The orthorhombic interface cell used is based upon the abrupt interface scheme described in the work of Devynck and Pasquarello^{43,58,59} and is extended to produce a 15 Å × 16 Å × 40 Å interface cell, with 20 Å of a-SiO₂. This approach produces an abrupt, defect free interface that well reproduces the interface bonding density and the experimentally observed band offsets. This allows us to consider particular interface defects individually, along with the influence of the local strain environment provided by the 3 bonding motifs. This formed the basis for all calculations allowing for the defect relaxation to be contained within the simulation supercell.

The defect electronic structure and HF parameters were calculated using the GAPW approximation in the CP2K code. The basis-sets appropriate for geometry optimizations are not valid for the calculation of hyperfine parameters, as an explicit description of the core electrons and hence an all electron basis set is required. Using the same approach and calibration set as outlined in Refs. 60-62, the pcj-3 basis set was selected for the HF calculations offering the best balance of speed and accuracy.⁶⁰

C. Defect calculations

The above parameters and supercells were used for all defect calculations. Initially, the neutral charge states were calculated, and from the number of occupied and unoccupied gap states, the accessible charge states for a given defect were inferred and calculated. The defect formation energy (E_f) was calculated using the standard formalism of Northrup and Zhang. Our calculations of E_f neglect the temperature dependent portion of the free energy of formation (Ω_f), which includes phonon effects that are challenging to calculate.⁶³ While E_f dominates at low temperatures, the entropy term can have a marked effect at elevated temperatures. However, explicit consideration is beyond the scope of this work, and here E_f is assumed to approximate Ω_f . The chemical potential is treated in line with the convention of Torpo *et al.*⁶⁴ and Knaup *et al.*⁹ It is important to note that the formation energy assumes that the system has reached thermodynamic equilibrium before meaningful concentration data can be extracted. Achieving thermodynamic equilibrium in the case of deposition and oxidation is far from assured. While the various post-oxidation anneals are expected to move the system closer to equilibrium and significant thermal budgets are provided (>1350 K), these temperatures are insufficient to remake the interface. This is not to say that useful information cannot still be extracted. Charge transition levels (CTLs) provide useful information on the most stable charge state (and multiplicity) for a given Fermi level position, while defect concentrations in this case cannot. The Lany-Zunger finite size charge correction scheme is utilized for all charged defects, and the magnitude of this correction is typically small (<0.1 eV) although it does become more significant in the higher charge states.⁶⁵

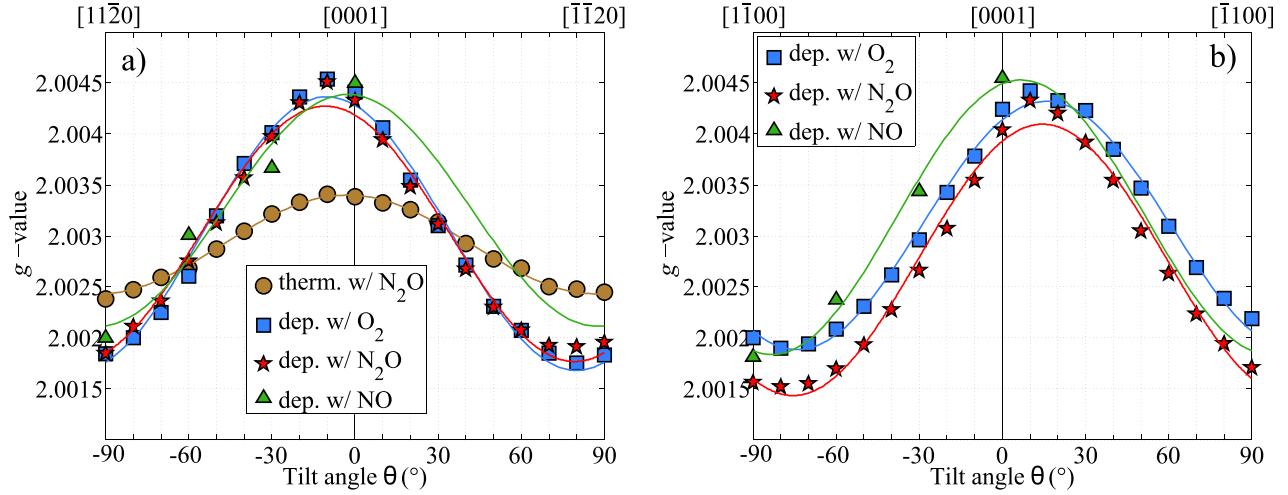


FIG. 1. Tilt series to show the angular dependence of the various anneals as detailed in the figure. The tilt goes over 180°, from $[11\bar{2}0]$ (-90°) to $[0001]$ (0°) to $[\bar{1}\bar{1}20]$ (90°) for (a), and from $[1\bar{1}00]$ (-90°) to $[0001]$ (0°) to $[\bar{1}\bar{1}00]$ (90°) for (b).

III. EXPERIMENTAL RESULTS

A. Angular dependence

The angular dependence of the signal of interest gives information on the symmetry of the defects and additionally allows for a comparison between devices. By changing the angle between the applied magnetic field and the sample, the angular dependence has been recorded, as shown in the tilt maps in Fig. 1. There is only a single orientation of the device with the thermal oxide and this is only included for completeness. Furthermore, this device is from an older generation of MOSFETs and possesses inferior device properties to the other devices, as shown in Table I. As such, it can be expected to have a significantly different interface to the other devices characterized here. For the NO sample, only a few points are recorded as extensive averaging was required to determine the g -factor due to the low defect density and small EDMR signal in this device. It is emphasized here that due to the broad linewidth of the EDMR spectra, no distinction between different defect sites could be made. Some broadening off the highly symmetric crystalline c -axis was observed, suggesting that the overlapping traces are splitting up. However, it was not possible to follow individual traces of different defects or sites. Therefore, the tilt maps shown display the average g -factor of possibly overlapping signals.

From Fig. 1, it is clear that there are marked differences between the anisotropy of the devices with thermal and deposited oxides, respectively, with the thermal oxide being the most isotropic. The three deposited oxides show

extremely similar g -tensors, and the defect is present at an interface that is relevant from a device perspective. Table II shows the principal g -factors derived from the tilt series. It is worth pointing out that the devices with the deposited oxide have their symmetry direction slightly tilted off the c -axis. This may be an indication of distortions at the interface or a preference for certain defect sites over others. However, also an overlap of different types of defects may be an explanation. Furthermore, it has been pointed out that the ferromagnetic Ni contacts of the devices may add to the observed g -factor variation.⁴⁸ Therefore, in all further discussion, the g -factors are only treated qualitatively.

B. Hyperfine structure

The HF structure of defects in the devices listed above was recorded and considered with B parallel to the $[0001]$ direction. While the other directions were recorded, insufficient resolution of the smaller HF features was attained off the highly symmetric c -direction. Due to the extremely low signal-to-noise ratio of the NO-annealed device, no meaningful HF peaks could be resolved and the device is left out of the discussion here, aside from stating that the defect symmetry is extremely similar to N_2O and O_2 -treated systems. Based upon the similar g -tensors, it is assumed that the same defects exist in differing concentrations in all samples with the deposited oxide. Each measurement was recorded at low microwave power (<10 mW) and high microwave power (>100 mW), shown in Fig. 2. The final point of note is that the spectra shown below have been shifted and normalized to allow for easier comparison of the HF parameters.^{27,48,50}

TABLE I. Important device parameters of the studied devices: low field mobility (μ_{lf}), density of interface traps (D_{it}), V_g as used in the EDMR experiments, and the resulting drain current I_d .

Sample (Anneal)	μ_{lf} ($\text{cm}^2 \text{V}^{-1} \text{s}^{-1}$)	D_{it} ($\text{cm}^{-2} \text{eV}^{-1}$)	V_g (V)	I_d (nA)
Thermal (N_2O)	< 0.1	n.a.	-1.5	7
Deposited (O_2)	0.1	2.3×10^{12}	-5.2	25
Deposited (N_2O)	2.2	1.7×10^{12}	-4.2	40
Deposited (NO)	17.6	2.9×10^{11}	-6.0	190

TABLE II. Principal g -factors from the tilt series in Fig. 1.

Sample (Anneal)	g_{xx}	g_{yy}	g_{zz}
Thermal (N_2O)	2.0024	...	2.0034
Deposited (O_2)	2.0016	2.0019	2.0045
Deposited (N_2O)	2.0014	2.0018	2.0043
Deposited (NO)	2.0018	2.0021	2.0045

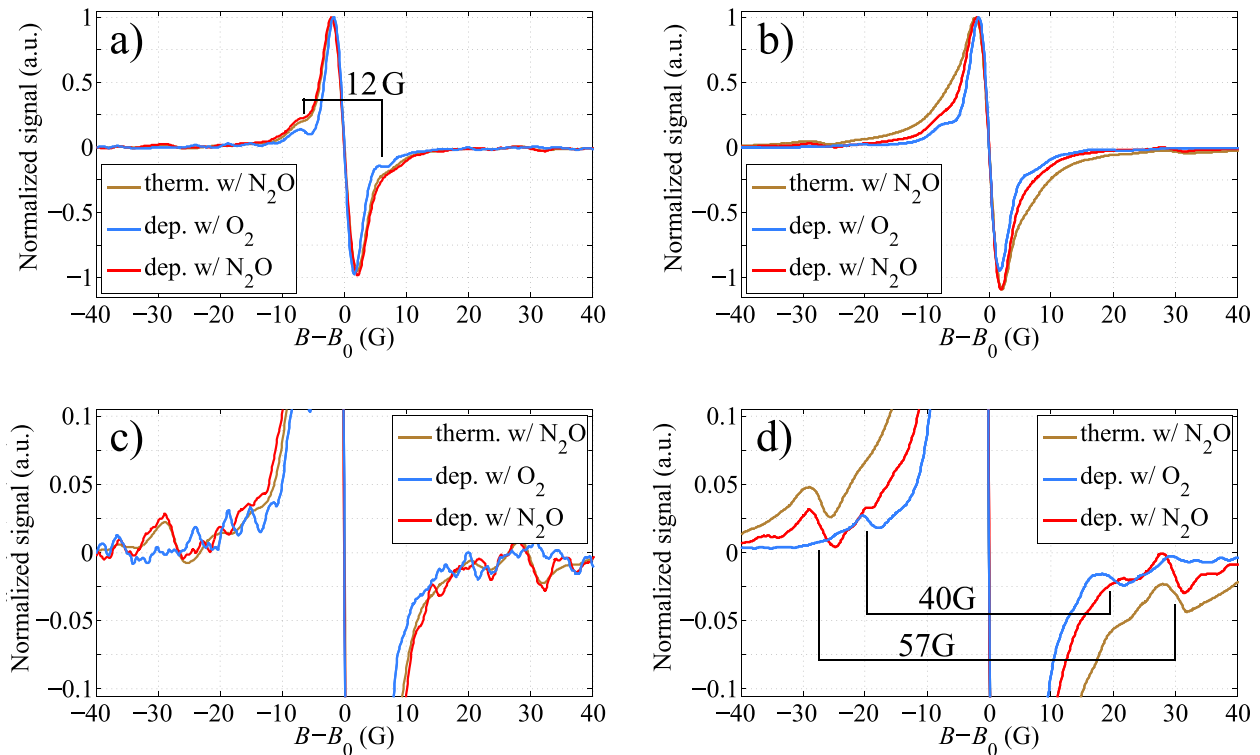


FIG. 2. A comparison of the HF-interactions of the dominant defect observed with EDMR as a result of the various passivation treatments. (a) The EDMR spectra of the indicated devices with a microwave power of $<10\text{ mW}$. (b) Gives the same spectra with a microwave power of $>100\text{ mW}$ and has the effect of broadening out the features. (c) and (d) A zoomed in view of (a) and (b), respectively, allowing the effect on the low intensity HF to be observed.

The main features that can be extracted from Fig. 2 are that the low power curves show clearly resolved HF peaks $\pm 6\text{ G}$ away from the center line, with a normalized intensity of 15%–20%. In the higher power measurements, these peaks are broadened to a point where they are no longer resolved in the N₂O devices. The O₂-treated device still shows the same peak in the high-power measurement, but with significant broadening. Note that this doublet is also observed at other tilt angles, indicating a low angular dependence of the HF splitting. Secondary features of lower intensity are observable in both the N₂O and the O₂-annealed devices, although the nature of these features appears to be distinct. In the N₂O devices, a doublet at $\pm 29\text{ G}$ is observed. However, this doublet was concluded to be due to a different unidentified defect, as it has a different angular behavior with respect to the center line and vanishes at elevated temperatures.^{27,50} This can be speculated to be an N-related or N-passivated defect, as it is only observed in the N-treated devices. However, further consideration of this defect is beyond the scope of this paper. In the O₂-annealed device, a low intensity peak ($\approx 1\%$) is observed at $\pm 20\text{ G}$, and this has the same center line and shows none of the angular quirks associated with the N-treated samples. However, this feature was only observable in the c -direction and after extensive signal averaging. This is an indication of overlapping spectra of differently oriented defects that are only equivalent in the c -direction. Therefore, when tilting away the individual spectra no longer overlap due to changing g -factors and HF splitting.

From consideration of the g -tensor and the HF behavior, it is possible to extract a “fingerprint” of the defect of

interest. The defect shows rotational symmetry about the crystal c -axis with a slight ($<10^\circ$) off axis tilt. Finally, from the HF interaction, there are two pronounced splittings of the center line, at $\pm 6\text{ G}$ with an intensity of approximately 15%, and at $\pm 20\text{ G}$ with an intensity of 1%–2%. These splittings were previously interpreted to be due to the Si and C splittings, respectively.⁴⁸

IV. THEORETICAL RESULTS

There are several studies in the literature that have described a number of defects that look extremely similar from an HF perspective to the defects described here, but show a g -value shift relative to one another.^{11–13,34,36–40,49,66} This is a counter intuitive state of affairs that has led to two interpretations. These defects appear to be most similar to the thermal oxide (with N₂O) described above, having the poorest interface quality, highest concentration of traps, and the most isotropic g -tensor (Table II). This is interpreted to be the negatively charged V_{Si} (V_{Si}^{-1}). This assignment is based on the average of the parallel and perpendicular g -values being that of the V_{Si} and the defect only having a small (or negligible) anisotropy.

The opposing viewpoint holds that the variation in g -value is an artifact of field, strain at the interface, or preparation, shifting B_{eff} and as such leading to the range of values shown above, although it is important to note that the origin of this shift is not well understood.⁴⁸ Taking the HF interaction and the angular behavior of the component parts into account, the alternative interpretation is the P_{bC} center or carbon dangling bond. It is important to consider here that it

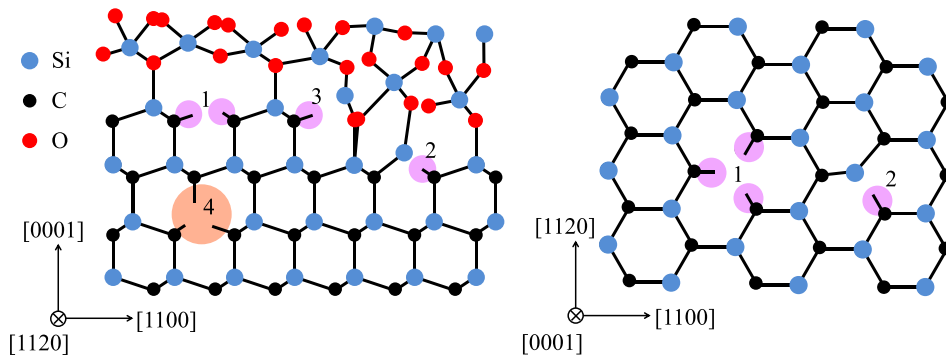


FIG. 3. Schematic view of the V_{Si} and the P_{bc} that are initially considered for comparison with the EDMR measurements. (1) V_{Si} on a terrace, (2) P_{bc} at a terrace, (3) P_{bc} on a step edge, and (4) V_{Si} in the layer beneath the interface. The blue circles represent Si, the black represent C, and red O.

is entirely reasonable to expect different defects to be present in different concentrations as a result of oxide formation and preparation. Both of the above candidates will be calculated and compared to the experimental data for the deposited oxide annealed in O_2 , as this gives a strong signal free of the artifacts present in the N-treated devices.

A. Interface defects

The defects previously postulated in the literature will form the starting point for the theoretical calculations and were considered using the interface model described above. The defects of interest are shown schematically in Fig. 3, highlighting the orientations of interest and how they are envisaged to fit into the 4H-SiC/SiO₂ interface context.

1. Silicon vacancy

The V_{Si} in the bulk SiC has been extensively characterized from both a theoretical and experimental perspective. In addition, the assignment of the bulk V_{Si} is universally agreed upon, as discussed above. Detailed consideration is beyond the scope of this work and the V_{Si} is only considered in the interface context (position 1 in Fig. 3). Additionally, only the simplest terrace interface morphologies are considered. We note that the local morphology would be expected to influence the local strain environment and by extension how the defect is able to relax.

The most pronounced effect of the interface upon the Si vacancy is to remove the upper most of the four C-dangling bonds. It breaks the symmetry of the bulk defect and is reduced to either C_{3v} when the interface allows for equivalent relaxation of the C-dangling bonds, or C_1 with three degenerate configurations, the principle symmetry axis being aligned along the crystal c -axis. This describes a defect with 3-fold rotational symmetry around the c -axis that is symmetric in the xy -plane and anisotropic with respect to the c -direction. Geometrically, the C-dangling bonds relax back into the plane of the neighboring Si, with a displacement of ≈ 0.2 – 0.4 Å compared to the unrelaxed geometry. The relaxation observed for the interface V_{Si} is significantly more pronounced ($\approx 50\%$) than for the bulk defect. As a result of this weak interaction between the V_{Si} dangling bonds, there is a small energy difference between the low spin (doublet) and the high spin (quartet), of the order of 0.2 eV in the neutral charge state. In the negative charge state, the high spin (triplet) is 0.1 eV lower in energy than the low spin (singlet).

The interface V_{Si} is accessible in the 0, -1 , and -2 charge states and in a variety of multiplicities. The doublet, triplet, and quartet states (Fig. 4) are all paramagnetic and hence would be visible to EDMR. The singlet states can be excluded as being invisible to EDMR. The -3 -charge state only becomes favorable at the 4H-SiC conduction band minimum (CBM) and is diamagnetic so has been omitted from Fig. 4. The first observation is that the moving of the V_{Si} from the bulk to the interface dramatically reduces the formation energy from ≈ 9 eV to 2 eV at the VBM. While caution is required in using formation energies in non-equilibrium conditions, the trend is clear. This can be understood as the V_{Si} being far easier to incorporate at the interface both electronically and sterically. From Fig. 4, the following CTLs can be extracted: (0/ -1) at 1.6 eV and (-1 / -2) at 2.9 eV. This describes a defect that is paramagnetic for the entire 4H-SiC band gap with the 0 and -1 charge states present in the observable region.

2. Carbon dangling bond (P_{bc})

The off-axis growth mechanism and the heavily stepped nature of the interface give rise to a large number of sites where the dangling bond could be envisaged to form. These are schematically illustrated in Fig. 3 as numbers 2 and 3, existing either at a step edge (3) or a dislocation between the oxide and SiC (2). These defects are a single sp^3 hybridized

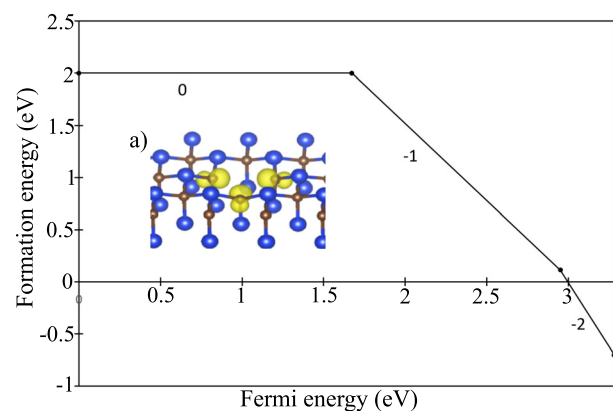


FIG. 4. Formation energy plot for the interface V_{Si} , showing the accessible charge states and CTLs within the SiC band gap. (a) The spin density of the V_{Si} in the neutral charge state at the SiC/SiO₂ interface; the oxide has been omitted from the picture for clarity. The spin density is indicated by the yellow lobes visualized with an isosurface of 0.07, Si blue, and C brown.

C-dangling bond, with a single electron in the neutral charge state. As described for the V_{Si} , the C-dangling bond relaxes back into the plane of the neighboring Si-atoms, the magnitude of the relaxation is less pronounced than with a displacement of 0.08 Å. With only a single C-dangling bond, there are only 2 accessible charge states, the 0 and -1 , with the 0 being favored for the majority of the SiC band gap. The formation energy plot is shown in Fig. 5. In this case, only the neutral charge state is paramagnetic with a $(0/-1)$ CTL at 1.9 eV. As the defect is principally localized on a single C-atom, there are no high spin variants to consider.

As with the V_{Si} configuration, steric environment and local strain play a limited role in the relaxation of the P_{bC} and the relative stability of the given charge states. The local strain environment affects the two neighboring Si atoms directly at the interface resulting in only a limited effect for the 3-coordinated C. To make sure a sufficient number of sites were considered, 30 different orientations of the P_{bC} were calculated. This provides an understanding of the effect of local strain environment on the defect relaxation. The variations in HF produced a direct probe of the geometric response of the variation in local strain environment and are highlighted in the [supplementary material](#).

From a configuration perspective, using Fig. 4 (V_{Si}) as a template, there are three degenerate orientations the P_{bC} may take, each being related by a 120° rotation about the c -axis. Additionally, due to the 4H-SiC crystal structure, the same three orientations are also present 60° rotated from each other, resulting in a total of six possible orientations of dangling bonds. These configurations are energetically equivalent for a given connection scheme; therefore, there is no strong tilt that would be observed in the EDMR measurements. This is in accordance with the observed in Fig. 1, with a tilt of $<10^\circ$. The tilt may be explained by unequal concentrations of the six possible configurations. As the wafers have been grown with a 4° off-axis tilt, the interface is heavily stepped, leading to both macro steps of several nanometers and steps of a few bilayers.

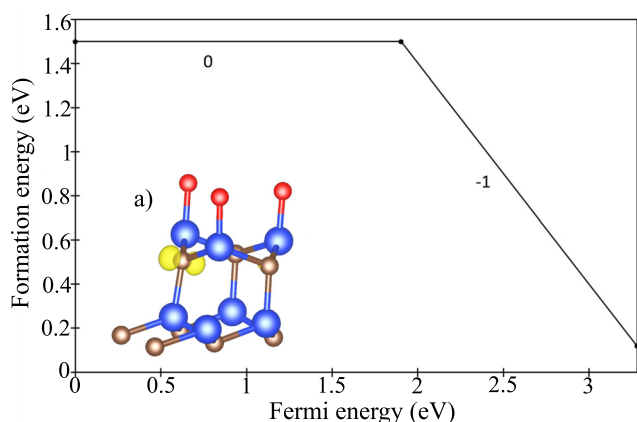


FIG. 5. Formation energy plot for a single configuration of the P_{bC} center, showing the accessible charge states and CTLs within the SiC band gap. (a) The geometry and the spin density of the P_{bC} predominately centered on the 3-coordinated C with the tails extending back to the neighboring atoms. The spin density is indicated by the yellow lobes visualized with an isosurface of 0.07. O is red, Si blue, and C brown.

3. Dual carbon dangling bond (Dual- P_{bC})

The final configuration of interest, the double carbon dangling bond, was found as a result of interface morphology investigations. As described by the previous TEM studies, including work on analogous devices, interface steps propagate in the $[\bar{1}100]$ direction, as this makes a diagonal cut across the surface.^{27,47} This gives rise to the possibility of both single dangling bonds (P_{bC}) and double dangling bonds (dual- P_{bC}). This defect can be formed in one of the two ways, either via partial oxidation or as a result of step bunching. Modeling the formation of this defect during the deposition and subsequent oxidative anneal is beyond the scope of this work and remains a challenge for the future work. The two configurations of this defect are shown in Fig. 6 and are made up of 2 adjacent weakly correlated P_{bC} defects, either at a step-edge [Fig. 6(a)] or as a result of partial oxidation on a terrace [Fig. 6(b)]. The step-edge dual- P_{bC} is created by removing the adjacent atoms and then H-capping of the facing Si-atoms, creating a single dual- P_{bC} at a step edge.

Both defects give a defect planar with respect to the interface (xy -plane) that like the P_{bC} can be viewed as a partially oxidized V_{Si} . The formation energy plot in Fig. 6 shows that the defect favors the 0 charge state, for the first half of the band gap, after which the -1 charge state is favored, for the region close the conduction band the -2 charge state becomes favored. The corresponding CTLs are $(0/-1)$ at 1.4 eV and $(-1/-2)$ at 3.0 eV. The defect configurations shown in Fig. 6 relax in a similar fashion, which is the same as described for the V_{Si} and the P_{bC} . The two C-dangling bonds relax back into the plane of the neighboring Si atoms, with a displacement of 0.1 Å compared to the unrelaxed structure.

The neutral charge state has a low spin (singlet) ground state and thus is diamagnetic and invisible to EDMR. However, as with the V_{Si} the weak interaction between C-dangling bonds leads to an energy difference of 0.04 eV between the singlet and the triplet. As a result, both need to be considered as the relative Boltzmann populations would be 84.4% and 15.6%, respectively, at room temperature.

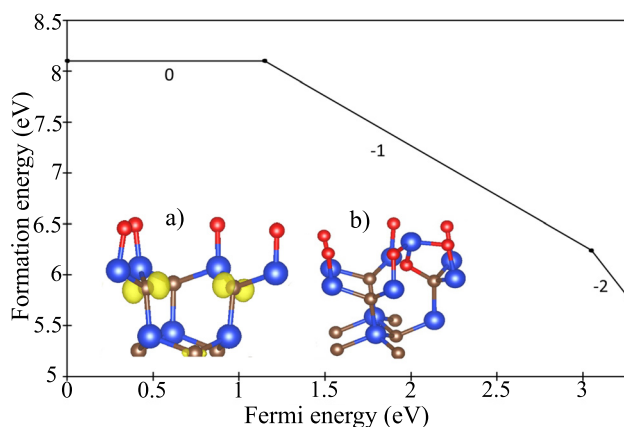


FIG. 6. Formation energy plot for the double dangling bond defect (dual- P_{bC}), showing the accessible charge states and CTLs within the SiC band gap. Inset, The dual- P_{bC} can exist in two forms that can be viewed as being a result of the stepped interface structure (a), or a result of partial oxidation (b). The spin density is indicated by the yellow lobes visualized with an isosurface of 0.07. In each case O is red, Si blue, and C brown.

TABLE III. Average HF splitting of the shortlisted defects for the defect center and concentric shells moving radial outwards for the [0001] direction. In the V_{Si} case there are $3 \times C_1$, $9 \times Si_2$ and $18 \times C_3$ the C_3 contribution tends to average to 0. The P_{bC} has $1 \times C_1$, $3 \times Si_2$, and $8 \times C_3$. The dual- P_{bC} has $2 \times C_1$, $6 \times Si_2$ and $16 \times C_3$.

Defect	C_1/G	Si_2/G	C_3/G
Surface- V_{Si}^0 (quartet)	35	8.5	1
Surface- V_{Si}^{-1} (triplet)	45	8.0	2
P_{bC}^0 (doublet)	39	12	2
Dual- P_{bC}^0 (triplet)	40	12	1
Dual- P_{bC}^{-1} (doublet)	39	10	1

The -1-charge state has a doublet ground state and is visible to EDMR.

V. COMPARISON BETWEEN THEORY AND EXPERIMENT

The defects described in Sec. IV allowed a shortlist to be identified for calculation of the HF parameters. These defects are the V_{Si}^0 , V_{Si}^{-1} , P_{bC}^0 , dual- P_{bC}^0 , dual- P_{bC}^{-1} . The calculated HF parameters for these defects are shown in Table III. These are the mean values averaged over multiple sites for each of the defect configurations, which allows the effect of local strain environment to be understood. Individual plots of the HF parameters of these configurations are presented in the [supplementary material](#). As described previously, only the Si-atoms directly at the interface show a sensitivity to the local strain environment, and the C-dangling bond is accommodated in the layer below the surface leading to only a limited impact. It is important to remember the limitations inherent in the abrupt model presented in this work, and it is possible for strain to have a more significant effect when step bunching is considered.

The V_{Si} shows a similar spectrum to the P_{bC} (Fig. 7), but the peak intensities are different as this is dictated by the isotopic abundance. The similarities between the defects here are to be expected as they are based upon very similar motifs, with varying numbers of carbon dangling bonds. The HF interactions in Table III show that for the 5 environments tested, they vary by less than 1 G exhibiting stability with respect to the different local strain environments.

Figure 8 shows the range of HF values that are calculated for the P_{bC} center as a result of the local strain environment. This is achieved by placing the defects at different positions at the interface, allowing the local strain environment to be probed. The C-HF values sit in a tight range between 36 and 44 G with the majority between 37 and 39 G; for the Si-HF values, a similar tight range is observed between 9 and 14 G. These values are tabulated in the [supplementary material](#) along with the individual plots. As is common for all the results here, a Gaussian broadening of 3 G is added to reflect the experimental conditions, room temperature, and an operating device. As there is no robust means of choosing between each of the dangling bond environments, a simple average is taken (Table III).

The final configuration is the dual- P_{bC} with the two accessible charge states showing very similar HF interactions

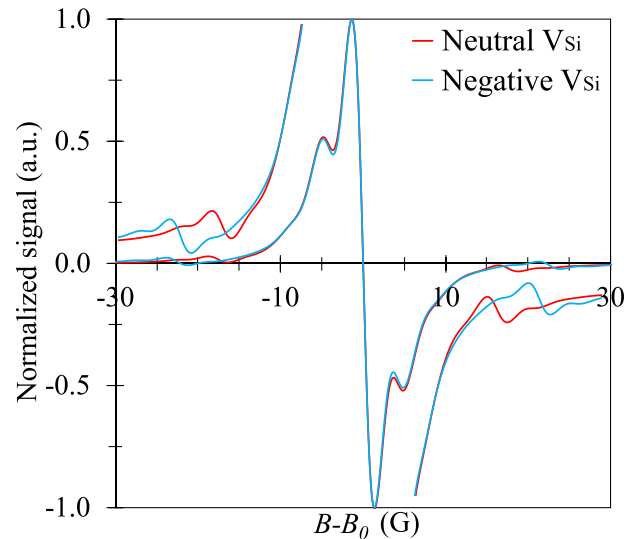


FIG. 7. The HF interaction for the interface V_{Si} in the neutral and negative charge states showing a similar a_{Si} regardless of charge state. In the case of the a_C a more pronounced shift is observed of ≈ 5 G between the charge states. The offset lines show a zoomed in view of the low intensity features.

with < 1 G deviation (Fig. 9). There are differences between the two configurations, and the a_{Si} shows a more pronounced broadening at the step edge (P_{bC} 2–2 from Fig. 9). This arises from a smaller Si-HF splitting, leading to the satellite peaks to merge into the center line. In the case of the C-HF, there is little deviation between the configurations with less than 0.5 G difference between the two sites. As with the P_{bC} , the two sites are averaged over as shown in Table III; similarly, there is no basis to balance between these sites using anything other than an equally weighted mean.

The defects shortlisted cannot be eliminated based upon an initial inspection of the HF parameters, as each defect is based upon varying numbers of the same motifs. For each of the above defects, plots are shown in Fig. 10. As before, no fitting parameters are used and 3 G broadening is added to reflect the measurements that were conducted at room temperature on operating devices. No probabilistic cut-offs are

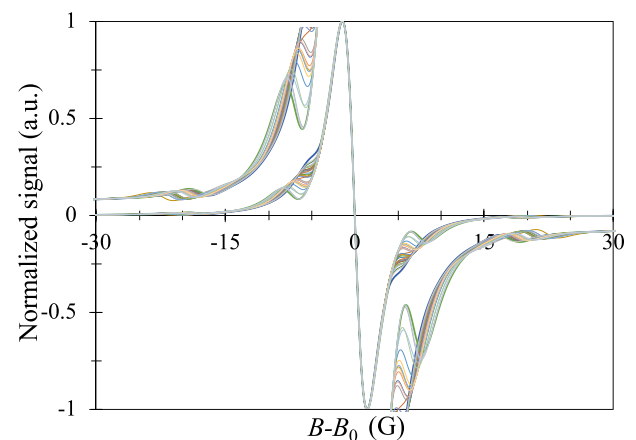


FIG. 8. The effect local strain environment has on the calculated HF interaction for the P_{bC} . The above values sit in a tight range of $a_C = \pm 4$ and $a_{Si} = \pm 2.5$ G. The apparent intensity shift arises from the merging of the shoulder features with the center line. The offset lines show a zoomed in view of the low intensity features.

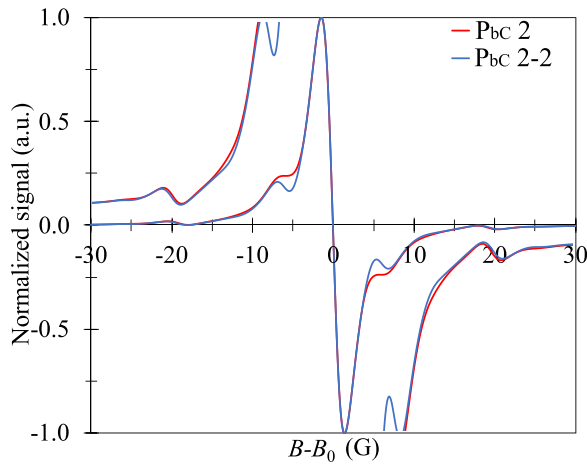


FIG. 9. HF interactions for the two charge states of the dual- P_{bC} , neutral triplet (P_{bC} 2-2) and negative doublet (P_{bC} 2). The offset lines show a zoomed in view of the low intensity features.

required when simulating the EPR spectrum in this case with all lines being considered. All of the spectra share some common features, as they are all based upon extremely similar motifs.

V_{Si} , in either of the charge states (Fig. 10), shows an HF splitting of approximately the correct magnitude $a_{Si} = \pm 4.25$ G. This agreement falls apart when the intensity of the peaks is considered based on the isotopic abundance of the spin active nuclei, relating to the probability of finding an isotope of non-zero nuclear spin at a given site. This intensity is only altered in samples that have in some way been enriched. The calculated values show that this is not the case here, with the values of a_{Si} falling into a tight range of ± 2.5 G. This excludes the V_{Si} as the defect solely responsible for the observed spectra.

As a result, the theoretical calculations rule out the interface V_{Si} in either charge state as the sole/major defect observed with EDMR in the current generation of nMOS devices. Additionally, as previously discussed, as the fast passage measurements identify a defect that is V_{Si} like, there must be two distinct recombination timescales involved. Only defects sensitive to the fast passage condition are probed by the fast passage technique. Defects not meeting this criterion are not probed, even if they represent an efficient recombination path. The fast passage defect is not directly studied here but does appear to match the model for the bulk V_{Si} .¹¹ This is clearly distinct from the defect identified in this study with conventional EDMR; this defect cannot be explained using any configuration or combination of configurations of the V_{Si} .^{11,48} While the magnitudes of the HF splittings are reasonable, the intensities are 2–3 \times greater than the observed, which in the absence of isotopic enrichment rules out the bulk and surface V_{Si} as the principle recombination defect observed *via* conventional EDMR. It is possible to view the P_{bC} and dual- P_{bC} as partially oxidized V_{Si} explaining the presence of a mixture of these defects at or around the interface.

For the P_{bC} and dual- P_{bC} centers (Fig. 10), the agreement is much more compelling, once again as with the V_{Si} the theoretical calculations give atomistic meaning to the

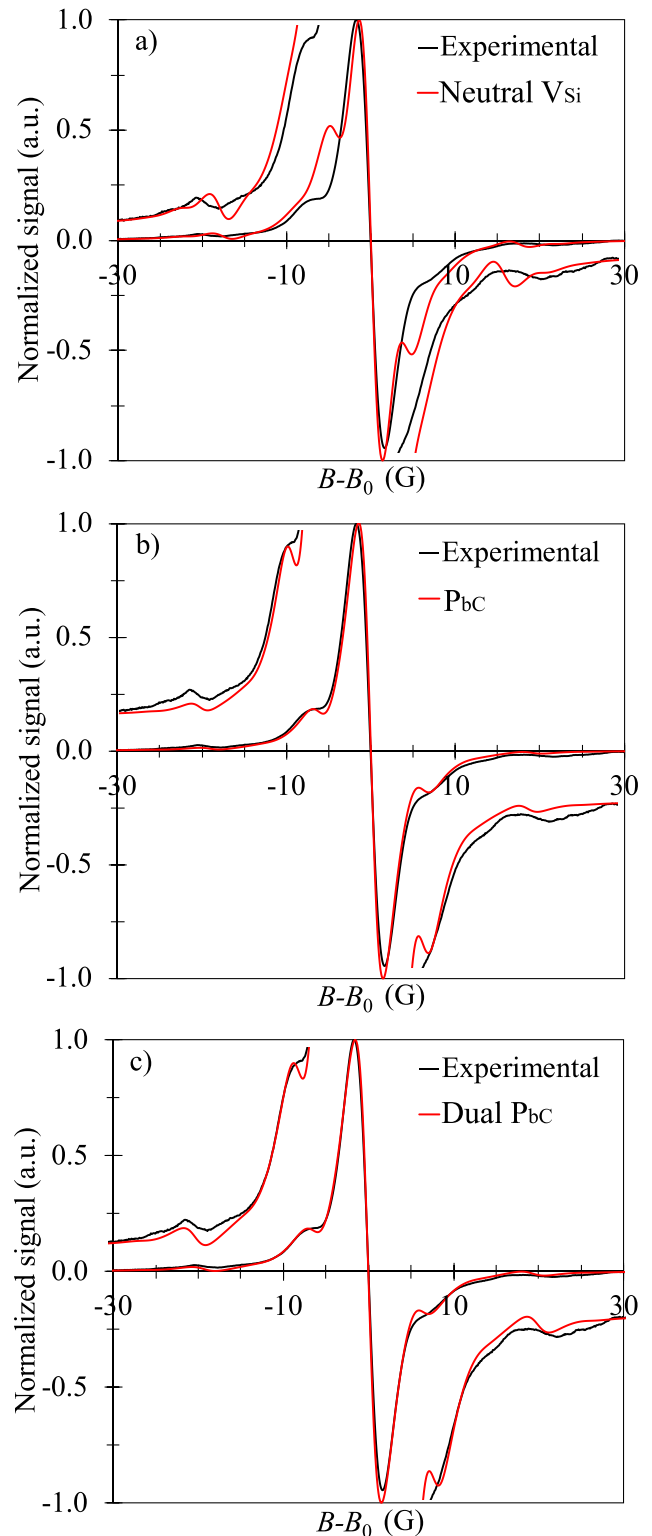


FIG. 10. A comparison of the EDMR spectra of candidate defects to the EDMR spectrum from the O_2 -annealed sample detailed in Fig. 2 and Table II. (a) V_{Si}^0 , (b) P_{bC}^0 , (c) dual- P_{bC} . The offset lines in each plot show a zoomed in view of the low intensity features.

experimental features. In this case, the 1%–2% intensity features at approximately ± 20 G relate to the splitting from the 3-coordinated C, accounting for 80% of the defect spin density. The narrow shoulder features with a 15%–20% intensity at ± 6 G relate to the splitting from the NN Si-atoms. The

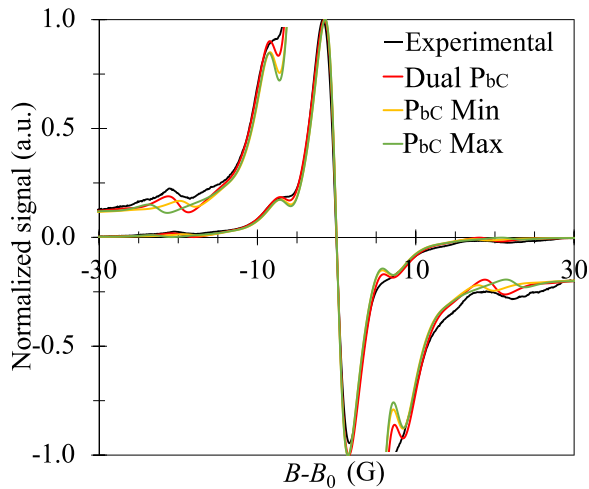


FIG. 11. A plot of the min-max C-HF interactions, along with the dual- P_{bc} showing an excellent agreement with the observed experimental data. In addition, the secondary features within the C-HF match the magnitude and intensity of the max-min P_{bc} values as a result. The offset lines show a zoomed in view of the low intensity features.

final shell of atoms with non-zero spin relates to the NNN C-atoms, and all of these splittings are below 1–2 G. As such, they contribute to the broadening, but the individual components cannot be resolved.

By considering both the averages [Figs. 10(b) and 10(c)] and expanding the picture to consider the Max-Min HF interactions (Fig. 11), both the P_{bc} and the dual- P_{bc} show excellent agreement with the experimental spectrum. Both the C-HF and the Si-HF interactions are very well reproduced, and the range relates to the majority of the defects having similar HF values, which are bracketed by the extreme values. This is far more pronounced in the C-HF values as the Si-HF sit in a much narrower range and is illustrated by the C-HF splitting shown in Fig. 11 where the secondary features of the C-HF are replicated by the extreme values calculated for the P_{bc} . The final part of the picture can be obtained by considering the V_{Si} close in the 5%–10% range; this provides a means of understanding the asymmetry present in the defect spectrum. By inspection this can be understood as the presence of an approximately isotropic defect with a center line offset by ≈ 2 G. This is shown in Fig. 12 and reproduces the observed asymmetry, along with the angular behavior of this under rotation, while it is important to stress that at this stage this can only be speculative as the line width is too broad to allow signal deconvolution to be achieved and the separate defect signals to be untangled.

This provides a possible explanation for the observed signal asymmetry, and more importantly, this reconciles the observation of the V_{Si} with fast passage and the dual- P_{bc}/P_{bc} with conventional EDMR.

It is tempting to take these results a stage further and infer relative concentration of each of the defect types and strain environments, and for EPR, this approach would be entirely justified. In the case of EDMR, this is not possible as the signal strength relates to the most effective recombination pathway and the concentration information is lost.

VI. CONCLUSION

Through the detailed comparison between the experimental EDMR measurements and *ab initio* calculations, the dominant EDMR active performance limiting recombination defect(s) observed with EDMR can be reasonably explained as a combination of the P_{bc} and the dual- P_{bc} defects. These defects match the symmetry, HF, and isotopic abundance observed in the experimental spectrum. Critically, this agreement is based upon no prior assumptions or fitting to achieve this agreement. This identifies a key performance limiting defect that is still prevalent in the current generation of devices, allowing the V_{Si} to be discounted as the main recombination defect in these devices, although still present in the current generation of devices and clearly present in the earlier devices. This supports the assignment of Cantin *et al.* for oxidized porous oxides, and the initial assignment of Gruber *et al.* for this system.^{12,48} In the context of the interface described for this generation of devices, the highly-stepped nature of the interface can be understood to give rise to a high number of sites where P_{bc} and dual- P_{bc} could be accommodated. Quantitatively, it is impossible to gauge the concentration of these sites; however, qualitatively from the previous TEM studies,^{25,27,32,47} the interface can be understood to be continuously stepped with a greater area than the observed terraces. Finally, it is interesting to note that there is a small asymmetry in the observed spectra which is consistent with minority population of an isotropic defect that is offset by approximately 2–3 G. This matches the g -value and the angular behavior of the V_{Si} at approximately 5%–10% of the intensity of the center line (P_{bc} & dual- P_{bc}). It is impossible to say with certainty how the interplay of the various contributions to this asymmetry is combined until higher resolution measurements are available. As device preparation has evolved, the sharpness of the interface appears to increase while becoming heavily stepped giving rise to the

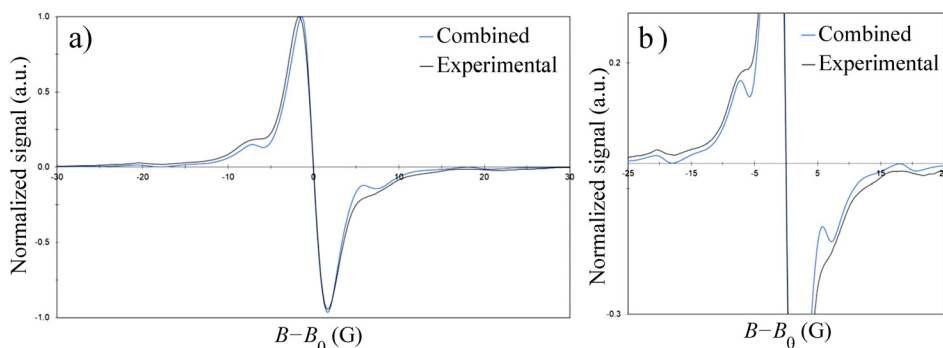


FIG. 12. A plot of the dual- P_{bc} and P_{bc} along with 5% of the V_{Si} . So the individual features are clearer and the Gaussian width is decreased to 2.5 G (zoomed in view of (a) is shown in (b)).

low coordinated sites where the P_{bc} family of defects can be expected to be found.

SUPPLEMENTARY MATERIAL

See [supplementary material](#) for the individual hyperfine parameters of the defects considered in this paper.

ACKNOWLEDGMENTS

J.C. and A.L.S. acknowledge the financial support from EPSRC (EP/G036675/1) for Centers for Doctoral Training scheme, Infineon Technologies AG, and the Leverhulme Trust (RPG-2016-135). The computational resources on Archer (<http://www.archer.ac.uk>) were provided via our membership of the UK's HEC Materials Chemistry Consortium, which is funded by EPSRC (EP/L000202). We would like to thank P. Deak, M. Bockstedte, and P. Lenahan for valuable comments and discussions.

- ¹T. Aichinger, G. Rescher, and G. Pobegen, *Microelectron. Rel.* **80**, 68 (2018).
- ²V. Presser and K. G. Nickel, *Crit. Rev. Solid State Mater. Sci.* **33**, 1 (2008).
- ³V. V. Afanas'ev and A. Stesmans, *Phys. Rev. Lett.* **78**, 2437 (1997).
- ⁴S. Wang, S. Dhar, S. R. Wang, A. C. Ahyi, A. Franceschetti, J. R. Williams, L. C. Feldman, and S. T. Pantelides, *Phys. Rev. Lett.* **98**, 026101 (2007).
- ⁵T. Umeda, J. Ishoya, T. Ohshima, N. Morishita, H. Itoh, and A. Gali, *Phys. Rev. B: Condens. Matter Mater. Phys.* **75**, 245202 (2007).
- ⁶T. Umeda, N. T. Son, J. Isoya, E. Janzén, T. Ohshima, N. Morishita, H. Itoh, A. Gali, and M. Bockstedte, *Phys. Rev. Lett.* **96**, 145501 (2006).
- ⁷T. Umeda, K. Esaki, R. Kosugi, K. Fukuda, N. Morishita, T. Ohshima, and J. Isoya, *Mater. Sci. Forum* **679–680**, 370 (2011).
- ⁸J. Isoya, T. Umeda, N. Mizuochi, N. T. Son, E. Janzén, and T. Ohshima, *Phys. Status Solidi B* **245**, 1298 (2008).
- ⁹J. M. Knaup, P. Deák, T. Frauenheim, A. Gali, Z. Hajnal, and W. J. Choyke, *Phys. Rev. B: Condens. Matter Mater. Phys.* **71**, 235321 (2005).
- ¹⁰A. Gali, T. Hornos, M. Bockstedte, and T. Frauenheim, *Mater. Sci. Forum* **556–557**, 439 (2007).
- ¹¹C. J. Cochrane, P. M. Lenahan, and A. J. Lelis, *Appl. Phys. Lett.* **100**, 023509 (2012).
- ¹²J. L. Cantin, H. J. von Bardeleben, Y. Shishkin, Y. Ke, R. P. Devaty, and W. J. Choyke, *Phys. Rev. Lett.* **92**, 015502 (2004).
- ¹³H. J. von Bardeleben, J. L. Cantin, L. Ke, Y. Shishkin, R. P. Devaty, and W. J. Choyke, *Mater. Sci. Forum* **483–485**, 273 (2005).
- ¹⁴S. Dimitrijević, *Mater. Sci. Forum* **457–460**, 1263 (2004).
- ¹⁵E. N. Kalabukhova, S. N. Lukin, D. V. Savchenko, B. D. Shanina, A. V. Vasin, V. S. Lysenko, A. N. Nazarov, A. V. Rusavsky, J. Hoentsch, and Y. Koshka, *Phys. Rev. B* **81**, 155319 (2010).
- ¹⁶N. Mizuochi, S. Yamasaki, H. Takizawa, N. Morishita, T. Ohshima, H. Itoh, and J. Isoya, *Phys. Rev. B* **68**, 165206 (2003).
- ¹⁷F. Amy, P. Soukiassian, Y. K. Hwu, and C. Brylinski, *Phys. Rev. B* **65**, 165323 (2000).
- ¹⁸S. H. Choi, D. Wang, J. R. Williams, M. Park, W. Lu, S. Dhar, and L. C. Feldman, *Appl. Surf. Sci.* **253**, 5411–5414 (2007).
- ¹⁹M. Maekawa, A. Kawasuso, M. Yoshikawa, A. Miyashita, R. Suzuki, and T. Ohdaira, *Phys. B: Condens. Matter* **376–377**, 354–357 (2006).
- ²⁰M. Maekawa, A. Kawasuso, M. Yoshikawa, and H. Itoh, *Appl. Surf. Sci.* **216**, 365–370 (2003).
- ²¹J. M. Powers and G. A. Somorjai, *Surf. Sci.* **244**, 39 (1991).
- ²²B. Hornetz, H.-J. Michel, and J. Halbritter, *J. Mater. Res.* **9**, 3088 (1994).
- ²³J. G. Li, *J. Am. Ceram. Soc.* **75**, 3118 (1992).
- ²⁴K. C. Chang, N. T. Nuhfer, L. M. Porter, and Q. Wahab, *Appl. Phys. Lett.* **77**, 2186 (2000).
- ²⁵C. Strenger, V. Häublein, T. Erlbacher, A. J. Bauer, H. Ryssel, A. M. Beltran, S. Schamm-Chardon, V. Mortet, E. Bedel-Pereira, M. Lefebvre, and F. Cristiano, *Mater. Sci. Forum* **717–720**, 437 (2012).
- ²⁶J. Houston Dycus, W. Xu, D. J. Lichtenwalner, B. Hull, J. W. Palmour, and J. M. LeBeau, *Appl. Phys. Lett.* **108**, 201607 (2016).
- ²⁷G. Gruber, “Performance and reliability limiting point defects in SiC power devices,” Ph.D. thesis (Technische Universität Graz, 2016).
- ²⁸T. Zheleva, A. Lelis, G. Duscher, F. Liu, I. Levin, and M. Das, *Appl. Phys. Lett.* **93**, 022108 (2008).
- ²⁹J. Rozen, “Electronic properties and reliability of the SiO₂/SiC interface,” Ph.D. thesis (Vanderbilt University, 2008).
- ³⁰G. Liu, A. C. Ahyi, Y. Xu, T. Isaacs-Smith, Y. K. Sharma, J. R. Williams, L. C. Feldman, and S. Dhar, *IEEE Electron Device Lett.* **34**, 181 (2013).
- ³¹C. Virojanadara and L. Johansson, *Surf. Sci.* **472**, L145 (2001).
- ³²G. Gruber, C. Gspan, E. Fisslthaler, M. Dienstleder, G. Pobegen, T. Aichinger, R. Meszaros, W. Grogger, and P. Hadley, *Adv. Mater. Interfaces* **5**, 1800022 (2018).
- ³³J. M. Knaup, P. Deák, T. Frauenheim, A. Gali, Z. Hajnal, and W. J. Choyke, *Phys. Rev. B: Condens. Matter Mater. Phys.* **72**, 115323 (2005).
- ³⁴H. J. von Bardeleben, J. Cantin, Y. Shishkin, R. P. Devaty, and W. Choyke, *Mater. Sci. Forum* **457–460**, 1457 (2004).
- ³⁵P. J. Macfarlane and M. E. Zvanut, *J. Appl. Phys.* **88**, 4122 (2000).
- ³⁶J. L. Cantin, H. J. Von Bardeleben, Y. Ke, R. P. Devaty, and W. J. Choyke, *Appl. Phys. Lett.* **88**, 092108 (2006).
- ³⁷C. J. Cochrane and P. M. Lenahan, *J. Magn. Reson.* **195**, 17 (2008).
- ³⁸C. J. Cochrane, P. M. Lenahan, J. P. Campbell, G. Bersuker, and A. Neugroschel, in *Proceedings of the IEEE International Integrated Reliability Workshop Final Report* (2006), p. 11.
- ³⁹C. J. Cochrane, P. M. Lenahan, and A. J. Lelis, *J. Appl. Phys.* **109**, 014506 (2011).
- ⁴⁰M. A. Anders, P. M. Lenahan, and A. J. Lelis, *Appl. Phys. Lett.* **109**, 142106 (2016).
- ⁴¹M. Weger, *Bell Syst. Tech. J.* **39**, 1013 (1960).
- ⁴²J. S. Hyde and L. Dalton, *Chem. Phys. Lett.* **16**, 568 (1972).
- ⁴³F. Devynck, A. Alkauskas, P. Broqvist, and A. Pasquarello, *Phys. Rev. B* **84**, 235320 (2011).
- ⁴⁴P. Deák, J. M. Knaup, T. Hornos, C. Thill, A. Gali, and T. Frauenheim, *J. Phys. D: Appl. Phys.* **40**, 6242 (2007).
- ⁴⁵G. Pensl, F. Ciobanu, T. Frank, D. Kirmse, M. Krieger, S. Reshanov, F. Schmid, M. Weidner, T. Ohshima, H. Itoh, and W. J. Choyke, *Microelectron. Eng.* **83**, 146 (2006).
- ⁴⁶M. Bassler, G. Pensl, and V. V. Afanas'ev, *Diamond Relat. Mater.* **6**, 1472 (1997).
- ⁴⁷P. Liu, G. Li, G. Duscher, Y. K. Sharma, A. C. Ahyi, T. Isaacs-Smith, J. R. Williams, and S. Dhar, *J. Vac. Sci. Technol. A* **32**, 060603 (2014).
- ⁴⁸G. Gruber, J. Cottom, R. Meszaros, M. Koch, G. Pobegen, T. Aichinger, D. Peters, and P. Hadley, *J. Appl. Phys.* **123**, 161514 (2018).
- ⁴⁹T. Aichinger and P. M. Lenahan, *Appl. Phys. Lett.* **101**, 83504 (2012).
- ⁵⁰G. Gruber, T. Aichinger, G. Pobegen, D. Peters, M. Koch, and P. Hadley, *Mater. Sci. Forum* **858**, 643 (2016).
- ⁵¹J. VandeVondele, M. Krack, F. Mohamed, M. Parrinello, T. Chassaing, and J. Hutter, *Comput. Phys. Commun.* **167**, 103 (2005).
- ⁵²J. Heyd, G. E. Scuseria, and M. Ernzerhof, *J. Chem. Phys.* **124**, 219906 (2006).
- ⁵³J. P. Perdew, K. Burke, and M. Ernzerhof, *Phys. Rev. Lett.* **77**, 3865 (1996).
- ⁵⁴K. Burke, F. G. Cruz, and K. C. Lam, *J. Chem. Phys.* **109**, 8161 (1998).
- ⁵⁵J. Hutter, M. Iannuzzi, F. Schiffrmann, and J. VandeVondele, *Wiley Interdiscip. Rev.: Comput. Mol. Sci.* **4**, 15–25 (2014).
- ⁵⁶J. VandeVondele and J. Hutter, *J. Chem. Phys.* **127**, 114105 (2007).
- ⁵⁷M. Guidon, J. Hutter, and J. VandeVondele, *J. Chem. Theory Comput.* **6**, 2348 (2010).
- ⁵⁸F. Devynck, F. Giustino, and A. Pasquarello, *Microelectron. Eng.* **80**, 38 (2005).
- ⁵⁹F. Devynck, F. Giustino, P. Broqvist, and A. Pasquarello, *Phys. Rev. B* **76**, 075351 (2007).
- ⁶⁰F. Jensen, *J. Chem. Theory Comput.* **2**, 1360 (2006).
- ⁶¹J. Cottom, G. Gruber, P. Hadley, M. Koch, G. Pobegen, T. Aichinger, and A. L. Shluger, *J. Appl. Phys.* **119**, 181507 (2016).
- ⁶²J. Cottom, G. Gruber, G. Pobegen, T. Aichinger, and A. L. Shluger, *Mater. Sci. Forum* **858**, 257 (2016).
- ⁶³S. B. Zhang and J. E. Northrup, *Phys. Rev. Lett.* **67**, 2339 (1991).
- ⁶⁴L. Torpo, M. Marlo, T. E. M. Staab, and R. M. Nieminen, *J. Phys.: Condens. Matter* **13**, 6203 (2001).
- ⁶⁵S. Lany and A. Zunger, *Modell. Simul. Mater. Sci. Eng.* **17**, 84002 (2009).
- ⁶⁶H. J. von Bardeleben, J. Cantin, M. Mynbaeva, and S. E. Saddow, *Mater. Sci. Forum* **433–436**, 495 (2003).